NOx Reduction in Diesel-Hydrogen Engines Using Different Strategies of Ammonia Injection

M. I. Lamas [1],* and C. G. Rodriguez [2]

[1] Nautical Sciences and Marine Engineering Department, Universidade da Coruña, 15403 Ferrol, Spain
[2] Norplan Engineering S.L., 15570 Naron, Spain; c.rodriguez.vidal@udc.es
* Correspondence: isabellamas@udc.es; Tel.: +34-881013896

check for updates

Abstract: In order to reduce NO_x emissions in internal combustion engines, the present work analyzes a measurement which consists of injecting ammonia directly into the combustion chamber. A commercial compression ignition engine fueled with a hydrogen-diesel blend was studied numerically. It was verified that the flow rate shape in which the ammonia was injected, particularly rectangular, triangular, or parabolic, as well as the injection duration had an important influence on NO_x reduction. A 11.4% improvement in NO_x reduction, corresponding to an overall reduction of 78.2% in NO_x, was found for parabolic injection shape and 1° injection duration. The effect on carbon dioxide, carbon monoxide, and hydrocarbon emissions, as well as brake-specific consumption, was negligible.

Keywords: CFD; NO_x; hydrogen; ammonia; engine

1. Introduction

Nowadays, it is very important to reduce emissions in internal combustion engines as well as the dependency on fossil fuels. The current concerns about the limitation of fossil fuels and pollution are strong incentives for finding alternative sources. In this regard, both hydrogen and ammonia constitute promising fuels because these may be produced from alternative sources [1]. Since ammonia and hydrogen are carbon-free, they do not produce carbon dioxide (CO_2), carbon monoxide (CO), unburned hydrocarbons (HC), nor particulates. Ammonia and hydrogen are also sulphur-free, and consequently, the emissions of sulphur oxides (SO_x) are also negligible, since these depend on the sulphur content in the fuel [2–5]. In internal combustion engines, ammonia-hydrogen blends complement their properties since ammonia is characterized by a narrow flammability range, high ignition energy, low combustion velocity, and high auto-ignition temperature. On the other hand, hydrogen presents a wide flammability range, low ignition energy, high combustion velocity, and lower auto-ignition temperature [6,7]. Besides, hydrogen can be obtained directly from ammonia [8–11]. Some investigations [12–15] proposed hydrogen as a promoter to speed up diesel-ammonia combustion. Technologically, the most employed option is to inject ammonia into the intake air. Boretti [16] analyzed several injection procedures in a dual fuel ammonia-hydrogen engine and concluded that the most adequate option is to inject ammonia into the intake air. Sahin et al. [17] analyzed ammonia injection into the intake air of a small engine and obtained advantages regarding efficiency and CO_2 emissions, but at expenses of increments in NO_x, HC, and CO. Reiter et al. [18] also employed injection of ammonia into the intake air of an engine and obtained a noticeable reduction in soot emissions but at the expense of increments in NO_x, HC, CO, and consumption. The authors indicated that the increment in NO_x emissions is mainly produced by ammonia oxidation. Nevertheless, they obtained that when less than 40% of the fuel energy is provided by ammonia, NO_x emissions are lower than for a diesel engine because the substitution by ammonia lowers the combustion temperature and thus reduces

the thermal NO_x formation mechanism. Another ammonia fumigation study was developed by Gill et al. [19], who injected ammonia and hydrogen into the intake air of a diesel engine and obtained reductions in consumption and CO_2 emissions as well as increments in HC and NO_x emissions.

Hydrogen usually increases NO_x emissions, especially at high loads, due to the high temperatures reached in the combustion chamber [20–22]. This constitutes an important problem, since the transport sector, especially internal combustion engines, is considered the major source of NO_x formation worldwide [23,24]. The production of NO_x from oxygen and nitrogen in the air is a problem associated to the combustion of fuels, and its reduction has been investigated for a long time. As a possible solution to reduce NO_x, hydrogen allows internal combustion engines to operate under ultra-lean combustion and thus under low-temperature combustion and lower NO_x emissions, but at the expense of reducing efficiency noticeably [25–27]. Other procedures to reduce NO_x emissions in internal combustion engines can be briefly summarized in primary and secondary measures. The latter consist of removing NO_x from the exhaust gases by downstream cleaning techniques, while the former consist of reducing NO_x produced during combustion by reducing the concentrations of oxygen and nitrogen as well as controlling the temperatures reached in the combustion process. The high price of after-treatment systems has promoted primary measures. In hydrogen engines, several techniques have been documented in the literature, such as modification of the injection parameters, reduction of the compression ratio, exhaust gas recirculation (EGR), water injection, etc.

As another measure to reduce NO_x emissions in hydrogen-ammonia engines, several authors proposed to inject ammonia directly into the cylinder during the expansion stroke. As this is a novelty and recent technology, the literature about direct ammonia injection is still scarce. One can refer to Miyamoto et al. [28], who analyzed a diesel engine and showed that NO_x emissions can be reduced by up to 60% by optimizing the injection timings. Larbi and Bessrorur [29] also found a substantial reduction in NO_x emissions by injecting ammonia directly into the combustion chamber. Lamas et al. [30] verified that ammonia injection is much more efficient than water injection to reduce NO_x.

Against this background, it can be concluded that an extended amount of literature has been developed on the applications of ammonia and hydrogen as fuels. Nevertheless, the research about direct ammonia injection into the combustion chamber as a NO_x reduction measure is still scarce. The present paper proposes a CFD (Computational Fluid Dynamics) model to analyze NO_x reduction in an internal combustion engine fueled with a hydrogen-diesel blend. Particularly, this work analyzes the commercial compression ignition engine MAN D2840LE V10. The process of NO_x reduction from ammonia injection directly into the combustion chamber was analyzed. Since ammonia is toxic, it is important to avoid un-reacted ammonia to slip into the atmosphere. For this reason, several injection shapes and durations were analyzed in order to optimize NO_x reduction and thus reduce ammonia slip.

2. Materials and Methods

The MAN D2840LE V10 analyzed, Figure 1, is a four-stroke, turbocharged, and direct injection engine. Table 1 summarizes the main technical specifications.

Figure 1. Engine analyzed in the present work.

Table 1. Technical specifications at 100% load.

Parameter	Value
Power (kW)	320
Speed (rpm)	1500
Number of cylinders	10
Cylinder displacement volume (cm^3)	18,270
Bore (mm)	128
Stroke (mm)	142

The photograph in Figure 2 illustrates the combustion chamber at the piston head. The computational grid is shown in Figure 3. A deforming mesh was employed in order to implement the movement to the piston and valves. Figure 3a represents the tri-dimensional grid at the bottom dead center and Figure 3b represents the AA cross section. All elements are hexahedral, and the mesh size was refined around the valves in order to adapt properly to their opening and closing. Several meshes with different elements and sizes were tested to verify the adequacy of the mesh.
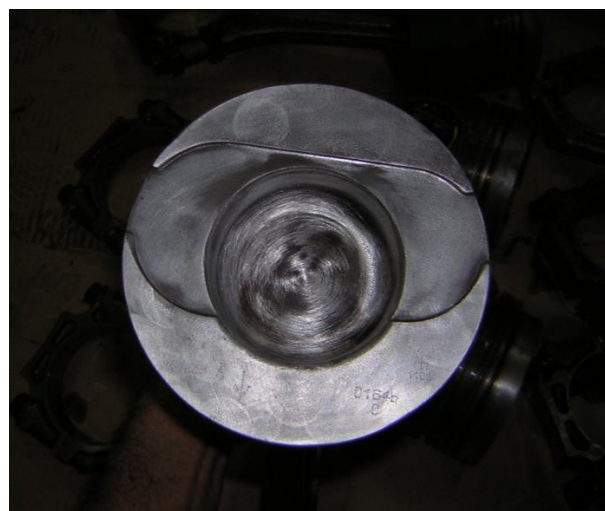

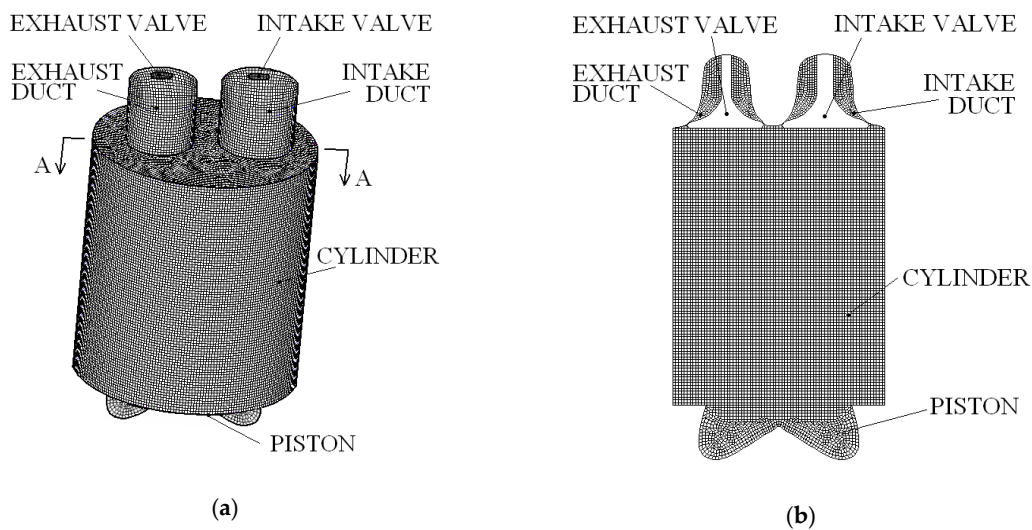**Figure 2.** Piston head of the engine studied in the present work.

Figure 3. Computational mesh at bottom dead center. (**a**) Tri-dimensional view; (**b**) AA section.

The open software OpenFOAM was employed for the simulations. A new in-house solver based on C++ language was programmed. The solver is based on the RANS (Reynolds-averaged Navier–Stokes) equations of conservation of mass, momentum, and energy, Equations (1)–(3).

$$\frac{\partial \rho}{\partial t} + \frac{\partial}{\partial x_i}(\rho u_i) = 0 \tag{1}$$

$$\frac{\partial}{\partial t}(\rho u_i) + \frac{\partial}{\partial x_j}(\rho u_i u_j) = -\frac{\partial p}{\partial x_i} + \frac{\partial \tau_{ij}}{\partial x_j} + \frac{\partial}{\partial x_j}(-\rho \overline{u_i' u_j'}) \tag{2}$$

$$\frac{\partial}{\partial t}(\rho H) + \frac{\partial}{\partial x_i}(\rho u_i H) = \frac{\partial}{\partial x_i}\left(\frac{\mu_t}{\sigma_t}\frac{\partial H}{\partial x_i}\right) + S_{rad} \tag{3}$$

In the equations above, ρ is the density, τ_{ij} is the viscous stress tensor, σ_t is the turbulent Prandtl number, μ_t is the turbulent viscosity, and H is the total enthalpy, computed by the sum of the enthalpy of all species. The enthalpy of each species was computed by

$$h_k = \int_{T_{ref}}^{T} c_{p,k} dT + h_k^0(T_{ref,k}) \tag{4}$$

where $c_{p,k}$ is the specific heat of species k, and h_k^0 is the formation enthalpy at the reference temperature $T_{ref,k}$.

The term S_{rad} in Equation (3) is a source to include radiation heat transfer. The P1 radiation model was employed, according to which the radiative source term for the enthalpy equation is:

$$S_{rad} = aG - 4a\sigma T^4 \tag{5}$$

where a is the absorption coefficient, 0.2 [31], and G is the incident radiation, obtained by the following transport equation:

$$\nabla \cdot \left(\frac{1}{3a}\nabla G\right) - aG + 4a\sigma T^4 = 0 \tag{6}$$

A common procedure to model the Reynolds stresses, $-\rho \overline{u_i' u_j'}$, is the Boussinesq hypothesis to relate the Reynolds stresses to the mean velocity gradients, Equation (7).

$$-\rho \overline{u_i' u_j'} = \mu_t \left(\frac{\partial u_i}{\partial x_j} + \frac{\partial u_j}{\partial x_i}\right) - \frac{2}{3}\rho k \delta_{ij} \tag{7}$$

where δ_{ij} is the Kronecker delta ($\delta_i = 1$ if $i = j$ and $\delta_i = 0$ if $i \neq j$), which is included to make the formula applicable to the normal Reynolds stresses for which $i = j$, Lamas and Rodriguez [32]. The turbulent viscosity was modeled by the *k-ε* turbulence model, according to which $\mu_t = \rho C_\mu k^2/\varepsilon$. The *k-ε* turbulence model implements two additional transport equations, one for the turbulence kinetic energy, *k*, Equation (8) and a further one for its dissipation rate, *ε*, Equation (9).

$$\frac{\partial}{\partial t}(\rho k) + \frac{\partial}{\partial x_i}(\rho k u_i) = \frac{\partial}{\partial x_j}\left(\frac{\mu_t}{\sigma_k}\frac{\partial k}{\partial x_j}\right) + 2\mu_t S_{ij} \cdot S_{ij} - \rho\varepsilon \tag{8}$$

$$\frac{\partial}{\partial t}(\rho\varepsilon) + \frac{\partial}{\partial x_i}(\rho\varepsilon u_i) = \frac{\partial}{\partial x_j}\left(\frac{\mu_t}{\sigma_\varepsilon}\frac{\partial\varepsilon}{\partial x_j}\right) + C_{1\varepsilon}\frac{\varepsilon}{k}2\mu_t S_{ij} \cdot S_{ij} - C_{2\varepsilon}\rho\frac{\varepsilon^2}{k} \tag{9}$$

In the equations above S_{ij} is the rate of deformation tensor, $C_{1\varepsilon}$ and $C_{2\varepsilon}$ are constants and the terms σ_k and σ_ε represent the turbulent Prandtl numbers for *k* and *ε*, respectively. The default values were assumed for the model constants, $C_\mu = 0.09$, $\sigma_k = 1.00$, $\sigma_\varepsilon = 1.30$, $C_{1\varepsilon} = 1.44$, and $C_{2\varepsilon} = 1.92$.

Regarding the simulation of fuel droplet breakup, the Kelvin-Helmholtz and Rayleigh-Taylor breakup models [33] were employed, and the heat-up and evaporation of the droplets was modeled by the Dukowicz model [34].

In order to solve the chemical kinetics, several additional equations must be added to the model. Given a set of *N* species and *m* reactions, Equation (10), the local mass fraction of each species, f_k, can be expressed by Equation (11).

$$\sum_{k=1}^{N} v'_{kj}M_k \overset{k_j}{\leftrightarrow} \sum_{k=1}^{N} v''_{kj}M_k \quad j = 1, 2, \ldots, m \tag{10}$$

$$\frac{\partial}{\partial t}(\rho f_k) + \frac{\partial}{\partial x_i}(\rho u_i f_k) = \frac{\partial}{\partial x_i}\left(\frac{\mu_t}{Sc_t}\frac{\partial f_k}{\partial x_i}\right) + S_k \tag{11}$$

In the equations above, v'_{kj} are the stoichiometric coefficients of the reactant species M_k in the reaction *j*, v''_{kj} is the stoichiometric coefficients of the product species M_k in the reaction *j*, Sc_t is the turbulent Smidth number, and S_k is the net rate of production of the species M_k by chemical reaction, given by the molecular weight multiplied by the production rate of the species, Equation (12),

$$S_k = MW_k\frac{d[M_k]}{dt} \tag{12}$$

where MW_k is the molecular weight of the species M_k and $[M_k]$ its concentration. The net progress rate is given by the production of the species M_k minus the destruction of the species M_k along the *m* reactions

$$\frac{d[M_k]}{dt} = \sum_{j=1}^{m}\left\{(v''_{kj} - v'_{kj})\left[k_{fj}\prod_{k=1}^{N}[M_k]^{v'_{kj}} - k_{bj}\prod_{k=1}^{N}[M_k]^{v''_{kj}}\right]\right\} \tag{13}$$

where k_{fj} and k_{fb} are the forward and backward reaction rate constants for each reaction *j*.

A reaction mechanism was programmed in the solver by integrating three kinetic schemes: combustion, NO_x formation, and NO_x reduction. Regarding NO_x reduction, the model of Miller and Glarborg [35], based on 24 species and 134 reactions, was employed. This model was validated with experimental results elsewhere [36], verifying that it reproduces the experimental trends with a reasonable accuracy. Regarding NO_x formation, the so-called extended Zeldovich mechanism is usually employed in CFD to characterize NO_x formation. This model is based on seven species and three reactions [37,38], listed in Appendix A.

Since the goal of the present work was to study NO_x, several NO_x formation mechanisms were developed and validated with experimental results using 100% diesel fuel. Gasboard-3000 (Wuhan Cubic) series gas analyzers were employed to characterize the composition of the exhaust

gas, particularly Gasboard-3030 for HC and Gasboard-3000 for NO, CO, and CO_2. This gas analyzer provides NO instead of NO_x, but the numerical model and numerous experimental analyses [39] indicated that NO_x is primarily NO. The extended Zeldovich model was compared to those of Mellor et al. [40], based on six reactions and eight species; Zabetta and Kilpinen [41], based on 10 reactions and 11 species; and Yang et al. [42], based on 20 species and 43 reactions, listed in Appendix B. The results obtained by these kinetic models at several loads and 1500 rpm are shown in Figure 4. This figure indicates that these models provide a satisfactory correspondence between numerical and experimental NO_x trends. Particularly, the extended Zeldovich model provides a 13.9% average error, while Mellor et al. [40] achieve 9.2%, Zabetta and Kilpinen [41] 8.1%, and Yang et al. [42] 5.8%. The R^2 resulted in 0.955, 0.958, 0.959, and 0.962 for the extended Zeldovich, Mellor et al. [40], Zabetta and Kilpinen [41], and Yang et al. [42] models, respectively. According to this, the model of Yang et al. [42] was used for the computations in the remainder of the present paper.
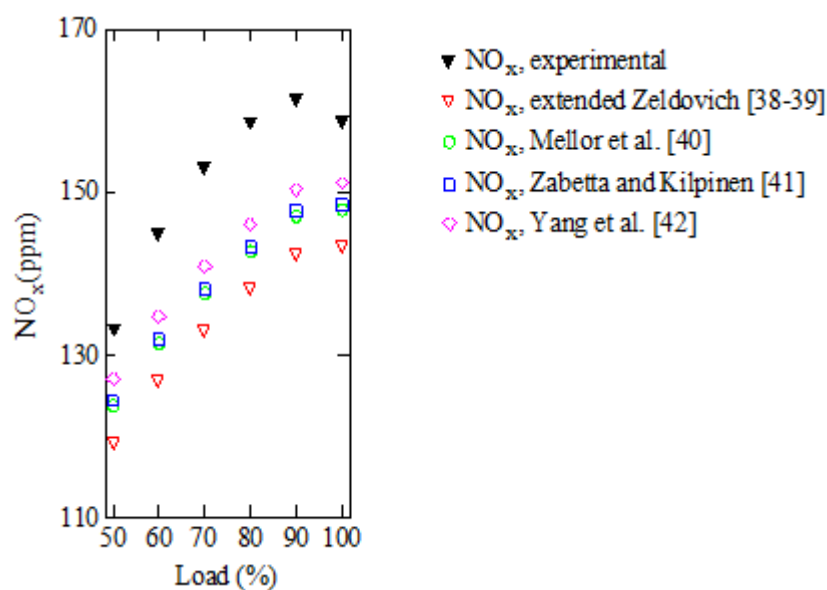

Figure 4. NO_x emissions experimentally and numerically obtained.

Regarding the combustion mechanism, the simplest procedure is to assume that the kinetics are so fast that chemical species remain at equilibrium [30,36,43]. This hypothesis is commonly used in CFD taking into account the high temperatures reached during combustion, which promote fast kinetics. Nevertheless, a kinetic scheme is more accurate than the equilibrium hypothesis since the warming in the expansion process of an engine and dilution with the excess air elongate the time needed to achieve equilibrium. For instance, in the case of CO and HC, one of the sources of formation are warm regions that are not able to burn properly. In this case, the chemical equilibrium hypothesis leads to overestimating the levels of these species. For this reason, a chemical kinetic model was employed in the present work. Particularly, Ra and Reitz's [44] model, based on 131 reactions and 41 species, was chosen. HC, CO, and CO_2 emissions as well as brake-specific fuel consumption at different loads and 1500 rpm are represented in Figure 5. This figure shows that a reasonable agreement was obtained, since the average error was 6.2%, 6.9%, 4.1%, and 3.8% for HC, CO, CO_2, and brake-specific fuel consumption (BSFC), respectively. Several reasons are responsible for the discrepancies between the numerical and experimental results obtained in Figures 4 and 5. Numerical techniques introduce inevitable errors due to the hypotheses assumed and the discretization on both the domain and governing equations. The RANS equations are time-averaged equations and the *k*-ε is a turbulence model that reproduces, as accurately as possible, the fluid flow. The P1 model for radiation, Kelvin-Helmholtz and Rayleigh-Taylor models for breakup, and Dukowicz model for heat-up and evaporation of the droplets are also models which reproduce, as accurately as possible, the

physical mechanisms. Besides, the kinetic models employed are simplifications of the tens of species and hundreds of reactions involved in the chemistry of combustion. More accurate turbulence models such as LES (Large Eddy Simulation) or DNS (Direct Numerical Simulation) are too computationally expensive, as is the simulation of the hundreds of reactions involved. With the advancement of computational resources, it is expected that in the near future it will be possible to employ more accurate turbulence models and more chemical reactions within a reasonable computational time.
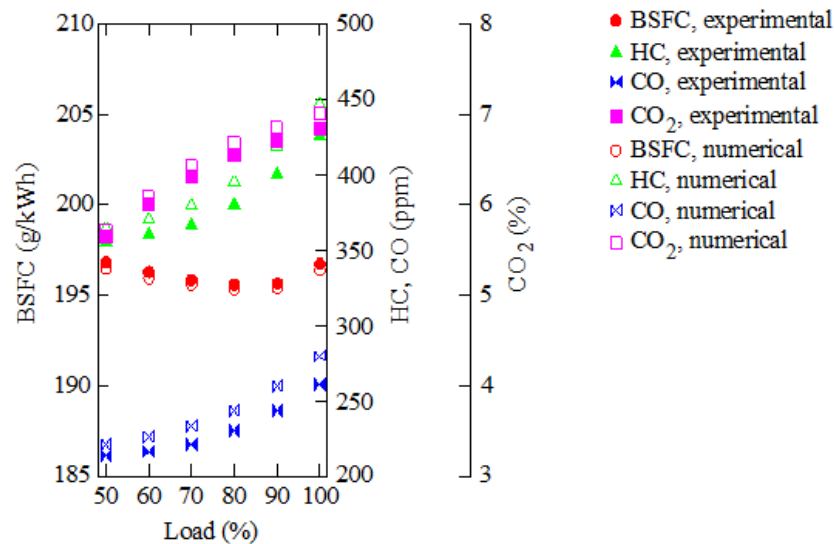

Figure 5. HC, CO, and CO_2 emissions as well as brake-specific fuel consumption (BSFC) experimentally and numerically obtained.

Regarding the simulation of fuel droplet breakup, the Kelvin-Helmholtz and Rayleigh-Taylor breakup models [33] were employed, and the heat-up and evaporation of the droplets were modeled by the Dukowicz model [34].

3. Results and Discussion

Once the numerical model was validated, it offered an efficient, cheap, and fast method to analyze the performance and emissions of the engine. In the present work, the model was employed to analyze several injection rate shapes, particularly rectangular, triangular, and parabolic. Before that, it was necessary to determine a proper NH_3/NO_i volumetric ratio, where NO_i is the NO concentration in the exhaust gas without ammonia injection. Figure 6 represents the NO_x reduction as well as the ammonia slip in the exhaust gas against the NH_3/NO_i ratio using a rectangular ammonia injection shape, start of ammonia injection 43.2º after top dead center at the end of compression stroke, and 10º injection duration. This figure shows that more NO_x reduction is obtained as NH_3 is increased. Due to the toxicity of ammonia, it is important to maintain low values of un-reacted ammonia slip to the exhaust. For this reason, a value of 2 was employed as a threshold for NH_3/NO_i in the remaining discussion of the present paper. Values between 2 and 3 are considered appropriate as well, since NO_x reduction levels off around 3. A value greater than 3 provides few improvements in NO_x reduction but a considerably higher amount of un-reacted ammonia slips into the atmosphere, since ammonia slip analyses showed a noticeable increment with an increasing NH_3/NO_i ratio.
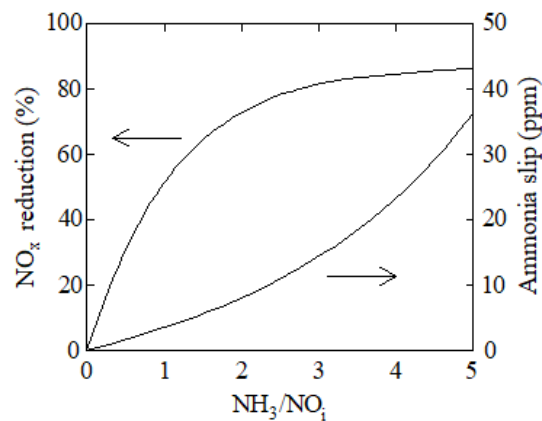
Figure 6. NO_x reduction against the NH_3/NO_i ratio. Start of ammonia injection 43.2°, 10° injection duration, rectangular injection shape.

Once the quantity of ammonia was determined, another important parameter to study was the shape of ammonia injection. The injection shapes indicated in Figure 7 were analyzed. These are rectangular, triangular, and parabolic. These three injection profiles refered to $NH_3/NO_i = 2$ and 10° injection duration. At 1500 rpm, 10° injection duration corresponded to 0.0011 s.
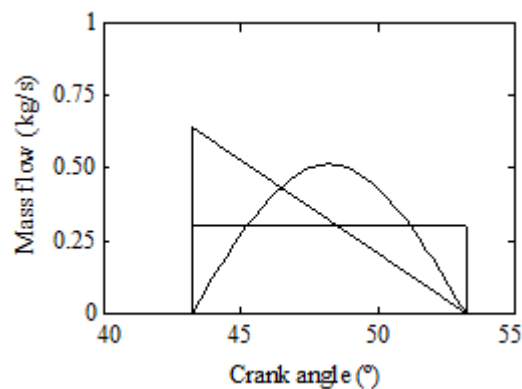

Figure 7. Ammonia injection rates analyzed.

The results for these three shapes are indicated in Figure 8, which illustrates the NO_x reduction against the start of ammonia injection using a 10° injection duration. This figure indicates that the instant start of ammonia injection has a noticeable effect on the NO_x reduction. The reason is that the process of NO_x reduction using ammonia is only efficient in a narrow temperature range. Consequently, in an internal combustion engine, it is too critical to determine the start of ammonia injection due to the variation of the in-cylinder temperature with the crankshaft angle. For the parameters analyzed in Figure 8, the maximum NO_x reduction was obtained at start of ammonia injections 43.2°, 45.8°, and 42.9° after top dead center at the end of compression stroke for rectangular, triangular, and parabolic injection shapes, respectively. The corresponding NO_x reductions were 68.3%, 66.8, and 71.1% for rectangular, triangular, and parabolic injection shapes, respectively. The reason which explains these differences is that high temperatures promote ammonia to oxidize to NO instead of reacting with NO, while at lower temperatures, the reduction reactions become slow and un-reacted ammonia can be emitted. According to this, the ammonia must be injected progressively from 0 to a maximum value and then decrease to 0 again. The parabolic shape is the shape that adapts more properly to this tendency while the triangular shape is the most different. Regarding brake-specific consumption and other emissions, such as CO, HC, and CO_2, it was verified that the effect was negligible.
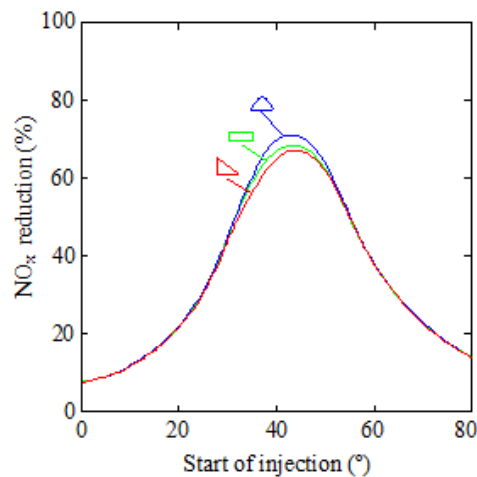
Figure 8. NO_x reduction against the start of ammonia injection for rectangular (green color), triangular (red color), and parabolic (blue color) injection shapes using 10° injection duration.

Another interesting parameter to analyze is the injection duration. Figure 9 shows the NO_x reduction against the duration of ammonia injection. In order to obtain these data, the ammonia injection was equally shortened at start and end, using the same quantity of ammonia injected. The maximum NO_x reduction obtained was 78.2%, corresponding to the parabolic shape at 1° injection duration. As can be seen in Figure 9, as the duration of ammonia injection was shortened, the NO_x reduction increased. The reason is that lower injection durations facilitate the supply of ammonia at the optimum crankshaft angle and thus at the optimum in-cylinder temperature. On the other hand, longer injections deviate more from the optimum crankshaft angle and thus from the optimum in-cylinder temperature to reduce NO_x. Particularly, from the data obtained from Figure 9, the NO_x reduction improved from 66.8% for the triangular shape with 10° injection duration to 78.2% for the parabolic shape with 1° injection duration; i.e., a 11.4% NO_x improvement was obtained. Another conclusion that can be obtained from Figure 9 is that the differences between rectangular, triangular, and parabolic shapes become smaller as the injection duration is reduced. The reason is that at shorter injection rates the ammonia is only injected at the optimum crankshaft angle and the injection duration is so short that the shape has a negligible influence. In practical applications, the injection rate can be shortened to the technically feasible level. Regarding brake-specific consumption and other emissions, such CO, HC, and CO_2, it was verified that the effect was negligible.
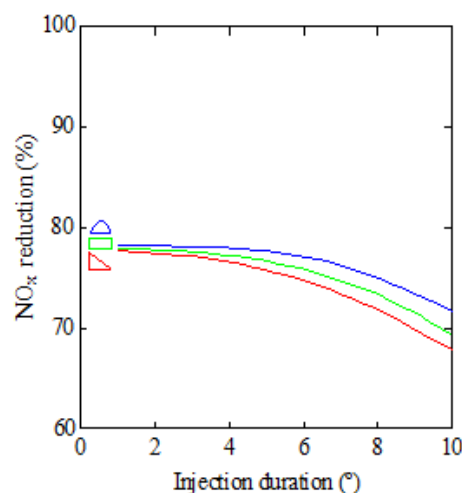

Figure 9. NO_x reduction against the duration of injection for rectangular (green color), triangular (red color), and parabolic (blue color) injection shapes.

4. Conclusions

This paper analyzes the capability of ammonia to reduce NO_x in a hydrogen-diesel engine. The motivation comes from the importance of the reduction of NO_x emissions which are usually produced when hydrogen is added to internal combustion engines, and the increasingly stringent NO_x restrictions. A CFD model was developed to analyze the commercial engine MAN D2840LE V10.

Since ammonia is toxic, it is important to optimize NO_x reduction, minimizing the un-reacted ammonia slipping into the atmosphere. According to this, a NH_3/NO_i proportion around 2 was considered adequate. It was verified that the NO_x reduction process using ammonia is highly dependent on the in-cylinder temperature. According to this, several ammonia injection shapes (rectangular, triangular, and parabolic) and durations (from 1º to 10º) were analyzed. The most appropriate case provided a 78.2% NO_x reduction using a parabolic injection shape and 1º injection duration. On the other hand, the worst case analyzed provided a 66.8% NO_x reduction using a triangular shape and 10º injection duration. As the injection duration is reduced, the differences between rectangular, triangular, and parabolic shapes become practically negligible. In practical applications, the injection rate can be shortened to the level that is technically feasible. For instance, in the present engine, which runs at 1500 rpm, 1º crankshaft angle corresponds to 0.00011 s. Current electromagnetic or solenoid injectors have longer response times but some piezo-injectors are able to switch on an off in tens of microseconds. These short injections provide practically identical results for rectangular, triangular, and parabolic injection shapes.

The main contribution of the present paper is that it provides a cheap and fast tool for studying NO_x reduction in internal combustion engines. This tool constitutes an alternative to expensive and laborious experimental tests. It can be employed to study the influence of parameters such as the exhaust and intake pressures, number and position of injectors, nozzles, injection pressure, cam profile design, compression ratio, etc.

In future works, the goal is to employ this numerical model to study other engine operation conditions and other emission reduction procedures, such as water addition, common rail, exhaust gas recirculation, etc. Furthermore, further important work is needed to develop more tests in this and other engines in order to obtain a more complete validation of the numerical model.

Conflicts of Interest: The authors declare no conflict of interest.

Appendix A

Reaction equations of the Zeldovich mechanism. The rate coefficients are in the form $k_f = AT^b e^{-E_0/T}$ (Table A1).

Table A1. Zeldovich mechanism.

	Reaction	A (cm^3/mol s)	b	E$_0$ (K)
1	$N_2 + O \leftrightarrow NO + N$	$1.800 \cdot 10^{14}$	0	38370
2	$N + O_2 \leftrightarrow NO + O$	$1.800 \cdot 10^{10}$	1	4680
3	$N + OH \leftrightarrow NO + H$	$7.100 \cdot 10^{13}$	0	450

Appendix B

Reaction equations of the Yang et al. [42] mechanism. The rate coefficients are in the form $k_f = AT^b e^{-E_0/T}$ (Table A2).

Table A2. Yang et al. [42] mechanism.

	Reaction	A (cm^3/mol s)	b	E$_0$ (K)
1	$N_2 + O \leftrightarrow NO + N$	$1.800 \cdot 10^{14}$	0.0	38370
2	$N + O_2 \leftrightarrow NO + O$	$1.800 \cdot 10^{10}$	1.0	4680
3	$N + OH \leftrightarrow NO + H$	$7.100 \cdot 10^{13}$	0.0	450
4	$N_2O + O \leftrightarrow 2NO$	$6.900 \cdot 10^{13}$	0.0	13400
5	$N_2O + O \leftrightarrow N_2 + O_2$	$1.000 \cdot 10^{14}$	0.0	14200
6	$N_2O + H \leftrightarrow N_2 + OH$	$7.587 \cdot 10^{13}$	0.0	7600
7	$N_2O + N_2 \leftrightarrow 2N_2 + O$	$6.918 \cdot 10^{23}$	−2.5	32170
8	$N_2O + N \leftrightarrow NO + N_2$	$1.000 \cdot 10^{13}$	0.0	10000
9	$N_2O + NO \leftrightarrow NO_2 + N_2$	$1.000 \cdot 10^{14}$	0.0	25000
10	$N_2O + O_2 \leftrightarrow NO + NO_2$	$6.000 \cdot 10^{14}$	−1.5	4985
11	$NO_2 + O \leftrightarrow NO + O_2$	$1.000 \cdot 10^{13}$	0.0	300
12	$NO_2 + H \leftrightarrow NO + OH$	$3.467 \cdot 10^{14}$	0.00	740
13	$NO_2 + NO_2 \leftrightarrow 2NO + O_2$	$1.995 \cdot 10^{12}$	0.00	13500
14	$NO_2 + N \leftrightarrow O + N_2O$	$5.012 \cdot 10^{12}$	0.0	0
15	$NO + HO_2 \leftrightarrow NO_2 + OH$	$2.089 \cdot 10^{12}$	0.0	−240
16	$NO + N_2 + O_2 \leftrightarrow N_2O + NO_2$	$2.300 \cdot 10^{14}$	0.0	18000
17	$N_2 + O_2 \leftrightarrow 2NO$	$2.730 \cdot 10^{13}$	0.0	53800
18	$NO + O_2 \leftrightarrow N + O_3$	$2.700 \cdot 10^{14}$	−1.0	63140
19	$NO_2 + O \leftrightarrow N + O_3$	$3.700 \cdot 10^{14}$	−0.5	40280
20	$NO + O_3 \leftrightarrow O + NO_3$	$6.000 \cdot 10^{14}$	−1.5	8000
21	$N_2 + HO_2 \leftrightarrow NO + HNO$	$5.925 \cdot 10^{10}$	0.5	21550
22	$N + OH \leftrightarrow NH + O$	$1.290 \cdot 10^{14}$	0.0	2165
23	$N + H_2 \leftrightarrow NH + H$	$1.320 \cdot 10^{15}$	0.0	11230
24	$N + H_2O \leftrightarrow NH + OH$	$3.590 \cdot 10^{15}$	0.0	18430
25	$NH + OH \leftrightarrow NO + H_2$	$1.600 \cdot 10^{12}$	0.56	755
26	$NH + O \leftrightarrow NO + H$	$5.000 \cdot 10^{11}$	0.5	0.0
27	$NH + OH \leftrightarrow HNO + H$	$6.440 \cdot 10^{11}$	0.0	1460
28	$NH + O_2 \leftrightarrow HNO + O$	$4.380 \cdot 10^{12}$	0.0	6546
29	$HNO \leftrightarrow H + NO$	$1.900 \cdot 10^{16}$	0.0	25179
30	$HNO + OH \leftrightarrow NO + H_2O$	$2.100 \cdot 10^{12}$	0.5	0
31	$HNO + H \leftrightarrow NO + H_2$	$1.400 \cdot 10^{13}$	0.0	1510
32	$HNO + O \leftrightarrow NO + OH$	$5.000 \cdot 10^{11}$	0.5	0
33	$NH + NO \leftrightarrow N_2O + H$	$2.240 \cdot 10^{13}$	0.0	10600
34	$N_2O + NH \leftrightarrow N_2 + HNO$	$1.995 \cdot 10^{12}$	0.0	3000
35	$NO_2 + NH \leftrightarrow HNO + NO$	$1.000 \cdot 10^{11}$	0.5	2000
36	$N + H_2O \leftrightarrow NH + OH$	$1.000 \cdot 10^{13}$	0.0	1000
37	$N + HO_2 \leftrightarrow NH + O_2$	$1.000 \cdot 10^{13}$	0.0	1000
38	$NO + HO_2 \leftrightarrow HNO + O$	$1.900 \cdot 10^{11}$	0.0	1000
39	$HNO + NO \leftrightarrow N_2O + OH$	$6.140 \cdot 10^{12}$	0.0	17100
40	$HNO + N \leftrightarrow NO + NH$	$1.000 \cdot 10^{13}$	0.0	1000
41	$HNO + HNO \leftrightarrow 2NO + H_2$	$2.000 \cdot 10^{10}$	0.5	2230
42	$NH + N \leftrightarrow N_2 + H$	$6.310 \cdot 10^{11}$	0.5	0
43	$NH + N_2 \leftrightarrow N + H + N_2$	$3.160 \cdot 10^{21}$	−2.0	42000

References

1. Seddiek, I.S.; Elgohary, M.M.; Ammar, N.R. The hydrogen-fuelled internal combustion engines for marine applications with a case study. *Brodogradnja* **2015**, *66*, 23–38.
2. Lamas, M.I.; Rodríguez, C.G.; Rodríguez, J.D.; Telmo, J. Internal modifications to reduce pollutant emissions from marine engines. A numerical approach. *J. Nav. Archit. Mar. Eng.* **2013**, *5*, 493–501. [CrossRef]

3. Seddiek, I.S.; Elgohary, M.M. Eco-friendly selection of ship emissions reduction strategies with emphasis on SOx and NOx emissions. *Int. J. Nav. Arch. Ocean Eng.* **2014**, *6*, 737–748. [CrossRef]

4. Ovaska, T.; Niemi, S.; Sirvio, K.; Nilson, O.; Portin, K.; Asplund, T. Effects of alternative marine diesel fuels on the exhaust particle size distributions of an off-road diesel engine. *Appl. Therm. Eng.* **2019**, *150*, 1168–1176. [CrossRef]

5. Abdulwahid, A.A.; Sigu, R.; Brown, R.J. Underground diesel exhaust wet scrubbers: Current status and future prospects. *Energies* **2018**, *11*, 3006. [CrossRef]

6. Frigo, S.; Gentili, R. Analysis of the behavior of a 4-stroke SI engine fuelled with ammonia and hydrogen. *Int. J. Hydrogen Energy* **2013**, *38*, 1607–1615. [CrossRef]

7. Reyes-Ramírez, I.; Martínez-Boggio, S.D.; Curto-Risso, P.L.; Medina, A.; Calvo Hernández, A.; Guzmán-Vargas, L. Symbolic analysis of the cycle-to-cycle variability of a gasoline–hydrogen fueled spark engine model. *Energies* **2018**, *11*, 968. [CrossRef]

8. Barrios, C.C.; Domínguez-Sáez, A.; Hormigo, D. Influence of hydrogen addition on combustion characteristics and particle number and size distribution emissions of a TDI diesel engine. *Fuel* **2017**, *199*, 162–168. [CrossRef]

9. Li, Y.; Chen, H.; Zhang, X.; Tan, C.; Ding, Y. Renewable energy carriers: Hydrogen or liquid air/nitrogen? *Appl. Therm. Eng.* **2010**, *30*, 1985–1990. [CrossRef]

10. Wang, W.; Herreros, J.M.; Tsolakis, A.; York, A.P.E. Ammonia as hydrogen carrier for transportation; investigation of the ammonia exhaust gas fuel reforming. *Int. J. Hydrogen Energy* **2013**, *38*, 9907–9917. [CrossRef]

11. Cervantes-Bobadilla, M.; Escobar-Jiménez, R.F.; Gómez-Aguilar, J.F.; García-Morales, J.; Olivares-Peregrino, V.H. Experimental study on the performance of controllers for the hydrogen gas production demanded by an internal combustion engine. *Energies* **2018**, *11*, 2157. [CrossRef]

12. Boretti, A. Novel dual fuel diesel-ammonia combustion system in advanced TDI engines. *Int. J. Hydrogen Energy* **2017**, *42*, 7071–7076. [CrossRef]

13. Comotti, M.; Frigo, S. Hydrogen generation system for ammonia-hydrogen fuelled internal combustion engines. *Int. J. Hydrogen Energy* **2015**, *40*, 10673–10686. [CrossRef]

14. Lee, J.H.; Kim, J.H.; Park, J.H.; Kwon, O.C. Studies on properties of laminar premixed hydrogen-added ammonia/air flames for hydrogen production. *Int. J. Hydrogen Energy* **2010**, *35*, 1054–1064. [CrossRef]

15. Ryu, K.; Zacharakis-Jutz, G.E.; Kong, S.C. Performance enhancement of ammonia-fueled engine by using dissociation catalyst for hydrogen generation. *Int. J. Hydrogen Energy* **2014**, *39*, 2390–2398. [CrossRef]

16. Boretti, A.A. Novel heavy duty engine concept for operation dual fuel H2-NH3. *Int. J. Hydrogen Energy* **2012**, *37*, 7869–7876. [CrossRef]

17. Sahin, Z.; Akcanca, I.Z.; Durgun, O. Experimental investigation of the effects of ammonia solution (NH3OH) on engine performance and exhaust emissions of a small diesel engine. *Fuel* **2018**, *214*, 330–341. [CrossRef]

18. Reiter, A.J.; Kong, S.C. Combustion and emissions characteristics of compression-ignition engine using dual ammonia-diesel fuel. *Fuel* **2011**, *90*, 87–97. [CrossRef]

19. Gill, S.S.; Chatha, G.S.; Tsolakis, A.; Golunski, S.E.; York, A.P.E. Assessing the effects of partially decarbonizing a diesel engine by co-fuelling with dissociated ammonia. *Int. J. Hydrogen Energy* **2012**, *37*, 6074–6083. [CrossRef]

20. Nishi, M.; Kanehara, M.; Lida, N. Assessment for innovative combustion on HCCI engine by controlling EGR ratio and engine speed. *Appl. Therm. Eng.* **2016**, *99*, 42–60. [CrossRef]

21. Wu, H.W.; Hsu, T.T.; He, J.Y.; Fan, C.M. optimal performance and emissions of diesel/hydrogen-rich gas engine varying intake air temperature and EGR ratio. *Appl. Therm. Eng.* **2017**, *124*, 381–392. [CrossRef]

22. di Sarli, V. Stability and emissions of a lean pre-mixed combustor with rich catalytic/lean-burn pilot. *Int. J. Chem. React. Eng.* **2014**, *12*, 77–89. [CrossRef]

23. Lamas, M.I.; Rodríguez, C.G.; Aas, H.P. Computational fluid dynamics analysis of NOx and other pollutants in the MAN B&W 7S50MC marine engine and effect of EGR and water addition. *Int. J. Marit. Eng.* **2013**, *155*, A81–A88.

24. Finesso, R.; Hardy, T.; Mancarella, A.; Marello, O.; Mittica, A.; Spessa, E. Real-time simulation of torque and nitrogen oxide emissions in a 11.0 L heavy-duty diesel engine for model-based combustion control. *Energies* **2019**, *12*, 460. [CrossRef]

25. Jasminska, N.; Brestovic, T.; Puskar, M.; Grega, R.; Rajzinger, J.; Korba, J. Evaluation of hydrogen storage capacities on individual adsorbents. *Meas. J. Int. Meas. Confed.* **2014**, *56*, 219–230. [CrossRef]

26. Lamas, M.I.; Rodríguez, J.d.; Castro-Santos, L.; Carral, L.M. Effect of multiple injection strategies on emissions and performance in the Wartsila 6L 46 marine engine. A numerical approach. *J. Clean. Prod.* **2019**, *206*, 1–10. [CrossRef]

27. Park, C.; Park, W.; Kim, Y.; Choi, Y.; Lim, B. Effect of valve timing and excess air ratio on torque in hydrogen-fueled internal combustion engine for UAV. *Energies* **2019**, *12*, 771. [CrossRef]

28. Miyamoto, N.; Ogawa, H.; Wang, J.; Shudo, T. Yamazaki K. Diesel NOx reduction with ammonium deoxidizing agents directly injected into the cylinder. *Int. J. Veh. Des.* **1995**, *16*, 71–79. [CrossRef]

29. Larbi, N.; Bessrour, J. Measurement and simulation of pollutant emissions from marine diesel combustion engine and their reduction by ammonia injection. *Adv. Mech. Eng.* **2010**, *41*, 898–906. [CrossRef]

30. Lamas, M.I.; Rodriguez, C.G.; Rodriguez, J.D.; Telmo, J. Computational fluid dynamics of NO_x reduction by ammonia injection in the MAN B&W 7S50MC marine engine. *Int. J. Marit. Eng.* **2014**, *156*, A213–A220. [CrossRef]

31. Bosse, T.K. *High Temperature Gas Dynamics*, 1st ed.; Springer: Berlin/Heidelberg, Germany; New York, NY, USA, 2004.

32. Lamas, M.I.; Rodríguez, C.G. CFD analysis of the scavenging process in the MAN B&W 7S50MC two-stroke diesel marine engine. *J. Ship Res.* **2012**, *56*, 154–161. [CrossRef]

33. Ricart, L.M.; Xin, J.; Bower, G.R.; Reitz, R.D. *In-Cylinder Measurement and Modeling of Liquid Fuel Spray Penetration in a Heavy-Duty Diesel Engine*; SAE 971591; SAE International: Warrendale, PA, USA, 1997.

34. Dukowicz, J.K. *Quasi-Steady Droplet Change in the Presence of Convection*; LA7997-MS; Informal Report Los Alamos Scientific Laboratory: Los Alamos, NM, USA, 1979.

35. Miller, J.A.; Glarborg, P. Modeling the formation of N2O and NO2 in the thermal DeNOx process. *Springer Ser. Chem. Phys.* **1996**, *61*, 318–333.

36. Lamas, M.; Rodriguez, C.G. Numerical model to analyze NO_x reduction by ammonia injection in diesel-hydrogen engines. *Int. J. Hydrogen Energy* **2017**, *42*, 26132–26141. [CrossRef]

37. Zeldovich, Y.B.; Sadovnikov, D.A.; Kamenetskii, F. *Oxidation of Nitrogen in Combustion*; Institute of Chemical Physics: Moscow-Leningrad, Russia, 1947.

38. Lavoie, G.A.; Heywood, J.B.; Keck, J.C. Experimental and theoretical investigation of nitric oxide formation in internal combustion engines. *Combust. Sci. Technol.* **1970**, *1*, 313–326. [CrossRef]

39. Woodyard, D. *Pounder's Marine Diesel Engines and Gas Turbines*, 8th ed.; Elsevier: Oxford, UK, 2004; ISBN 9780080943619.

40. Mellor, A.M. *Skeletal Mechanism for NOx Chemistry in Diesel Engines*; SAE Tech Pap 981450; SAE International: Warrendale, PA, USA, 1998.

41. Zabetta, E.C.; Kilpinen, P.; Hupa, M.; Stähl, K.; Leppälahti, J.; Cannon, M.; Nieminen, J. Kinetic modeling study on the potential of staged combustion in gas turbines for the reduction of nitrogen oxide emissions from biomass IGCC plants. *Energy Fuels* **2000**, *14*, 751–761. [CrossRef]

42. Yang, H.; Krishnan, S.R.; Srinivasan, K.K.; Midkiff, K.C. Modeling of NOx emissions using a super-extended Zeldovich mechanism. In Proceedings of the ICEF03 2003 Fall Technical Conference of the ASME Internal Combustion Engine Division, Erie, PA, USA, 7–10 September 2003.

43. Lamas, M.I.; Rodríguez, C.G. Numerical model to study the combustion process and emissions in the Wärtsilä 6L 46 four-stroke marine engine. *Pol. Marit. Res.* **2013**, *20*, 61–66. [CrossRef]

44. Ra, Y.; Reitz, R. A reduced chemical kinetic model for IC engine combustion simulations with primary reference fuels. *Combust. Flame* **2008**, *155*, 713–738. [CrossRef]